Scale- and load-dependent friction in commensurate sphere-on-flat contacts

Tristan A. Sharp, Lars Pastewka, Vincent L. Lignères, and Mark O. Robbins

Phys. Rev. B **96**, 155436 — Published 16 October 2017

DOI: 10.1103/PhysRevB.96.155436

Scale and load dependent friction in commensurate sphere-on-flat contacts

Tristan A. Sharp,[1,2] Lars Pastewka,[1,3,*] Vincent L. Lignères,[1] and Mark O. Robbins[1,†]

[1]*Department of Physics and Astronomy, Johns Hopkins University, 3400 North Charles Street, Baltimore, MD 21218, USA*
[2]*Department of Physics, University of Pennsylvania, 209 South 33rd Street, Philadelphai, PA 19104, USA*
[3]*Department of Microsystems Engineering, University of Freiburg, Georges-Köhler-Allee 103, 79110 Freiburg, Germany*

(Dated: September 18, 2017)

Contact of a spherical tip with a flat elastic substrate is simulated with a Green's function method that includes atomic structure at the interface while capturing elastic deformation in a semi-infinite substrate. The tip and substrate have identical crystal structures with nearest-neighbor spacing d and are aligned in registry. Purely repulsive interactions between surface atoms lead to a local shear strength that is the local pressure times a constant local friction coefficient α. The total friction between tip and substrate is calculated as a function of contact radius a and sphere radius R, with a up to $10^3 d$ and R up to $4 \times 10^4 d$. Three regimes are identified depending on the ratio of a to the core width of edge dislocations in the center of the contact. This ratio is proportional to $\alpha a^2/Rd$. In small contacts, all atoms move coherently and the total friction coefficient $\mu = \alpha$. When the contact radius exceeds the core width, a dislocation nucleates at the edge of the contact and rapidly advances to the center where it annihilates. The friction coefficient falls as $\mu \sim \alpha(\alpha a^2/Rd)^{-2/3}$. An array of dislocations forms in very large contacts and the friction is determined by the Peierls stress for dislocation motion. The Peierls stress rises with pressure, and μ rises with increasing load.

PACS numbers:
Keywords:

I. INTRODUCTION

The canonical geometry of tribology is a sphere contacting a flat surface.[1,2] This simple geometry is used for tribological testing, is found in ball bearings and many other mechanical devices, and is exploited in scanning probe metrology such as atomic force microscopy (AFM),[3] colloidal probe measurements[4] or in the surface force apparatus (SFA).[5] It is also often used to model each asperity in multi-asperity contacts between rough surfaces.[6] In this paper we show that atomistic effects can lead to complex, scale-dependent frictional behavior even for this simple geometry.

Continuum analyses of sphere-on-flat sliding can be found in many textbooks.[1,2,7] These models use standard elastic or plastic treatments of the bulk deformation combined with some assumption about the nature of the local interfacial shear strength. They then determine how the average static friction F_s scales with the load F_z pushing surfaces together and the contact area A.

One of the most common models, Cattaneo-Mindlin,[2] assumes a local coefficient of friction, i.e. that the maximum local shear stress at the interface $\tau_{\max}$ is proportional to the local pressure p: $\tau_{\max} = \alpha p$. If sliding occurs whenever the local shear stress exceeds $\tau_{\max}$, one finds that the static friction obeys Amontons' law: $F_s = \mu F_z$, where the coefficient of friction $\mu = \alpha$. In contrast, for adhesive surfaces $\tau_{\max}$ is usually assumed to be independent of pressure. In this case one finds a constant frictional shear stress $\tau_{\rm fric} \equiv F_s/A$ with $\tau_{\rm fric} = \tau_{\max}$. Both types of scaling have been observed in single-asperity friction experiments.[1,5,8–13]

In contrast to these classic continuum results, Hurtado and Kim[14,15] found that atomic surface structure could lead to striking scale-dependent friction laws. They considered crystalline surfaces that locked together in perfect registry to produce a load and area independent $\tau_{\max}$. The friction force on a circular contact of radius a was calculated using a dislocation model. For small radius $\tau_{\rm fric} = \tau_{\max}$, but larger contacts advance by dislocation motion and $\tau_{\rm fric}$ decreases as $a^{-1/2}$. At very large scales there are many dislocations and $\tau_{\rm fric}$ saturates once more at the Peierls stress,[16] $\tau_{\rm Peierls}$, for dislocation motion.

Experimental tests of Hurtado and Kim's results are complicated because they require atomically flat surfaces with a wide range of curvatures that lock in registry. The motivation of their work was to explain the higher frictional stresses in small AFM tips than in larger SFA experiments, but this difference can also be explained by the very different mechanical properties of the contacting materials in the references they cited.[9–11,17] Moreover, these experiments were performed with unaligned crystalline surfaces that were in general out of registry.

Testing Hurtado and Kim's model numerically is also challenging, because of the need to simulate large systems while maintaining atomic-scale resolution in the contact. Gao[18] used a Peierls-Nabarro model of a dislocation field at the interface to test Hurtado and Kim's model. The Peierls-Nabarro model was designed for lattice dislocations within a uniform bulk crystal rather than the case of contact with a curved surface. It simplifies atomic motion to two-dimensional displacements of substrate atoms in a periodic potential with a maxiumum shear stress $\tau_{\max}$

that is independent of load and area. Gao[18] observed the crossover from a constant $\tau_{\rm fric} = \tau_{\rm max}$ to a shear stress that dropped as $a^{-1/2}$.

More recently we used a Green's function approach[19,20] to capture the elastic response of a semi-infinite substrate while following individual atoms in contacts up to 2048 atoms across.[21] The results confirmed Hurtado and Kim's model for identical crystal surfaces, including the $a^{-1/2}$ scaling at intermediate scales and the saturation of $\tau_{\rm fric}$ at large scales. The dimensionless control parameter is the ratio $a/b_{\rm core}$ where $b_{\rm core}$ is the width of an interfacial dislocation. We also considered the more typical case of incommensurate contacts, where the crystalline substrate and tip share no common periodicity. Rigid incommensurate surfaces cannot lock in registry, and $\tau_{\rm fric}$ is predicted[22–24] to vanish as $a \to \infty$. However we found that dislocations can allow large contacts to lock, yielding a value of $\tau_{\rm fric} \approx \tau_{\rm Peierls}$ equal to that for very large identical, aligned crystals.[21]

Hurtado and Kim's model and previous numerical tests considered systems with a constant local shear stress $\tau_{\rm max}$ and simplified the problem by removing the local curvature of the surface. At high loads and for nonadhesive surfaces atomistic simulations show that the local frictional stress is proportional to pressure,[25–27] yielding a constant local friction coefficient $\alpha = \tau_{\rm max}/p$ rather than a constant shear stress. Since the pressure varies from zero at the contact radius to a maximum at the center of the contact, there is a large variation in the local friction force.

In this paper we present results from an explicit 3D simulation of atoms on a sphere of radius R contacting a flat elastic substrate. The purely repulsive interaction between surface atoms naturally leads to a local friction coefficient α. We find that results for different loads and R can be collapsed when plotted against $\alpha a^2/Rd$ where d is the atomic separation. By considering the scaling of $\tau_{\rm max} = \alpha p$ with a we show that this dimensionless parameter also corresponds to the ratio of a to a representative dislocation core width, which now depends on p. To isolate the effect of curvature, we also consider a modified Peierls-Nabarro model where the surface is flat but the local $\tau_{\rm max}$ follows the pressure distribution for a Hertzian contact. This simple model shows the same scaling of friction with sphere and contact radii as the explicit simulation.

The Green's function approach allows us to treat a/d up to 10^3 and R/d up to 10^5. At small a there is a constant coefficient of friction. At larger a, $\mu \propto a^{-4/3}$ and we show that this power law can be derived from a dislocation nucleation model. At the largest a, μ begins to rise once more. In this regime, μ is related to the Peierls stress for dislocations which grows with increasing normal load.

II. SIMULATION METHODS

A. Explicit Atomistic Model

Our explicit simulations consider quasi-static sliding of a rigid spherical tip over a flat semi-infinite elastic substrate, as illustrated in Fig. 1(a). Holding the spherical tip rigid reduces the number of parameters, and this geometry can be mapped to the sliding of two elastic, curved surfaces in continuum theory.[2] Continuum theory assumes small surface slopes. The maximum slope in a sphere on flat contact is a/R and we only show results from the explicit model with $a/R < 0.1$.

The substrate is the (100) surface of an fcc crystal with nearest-neighbor spacing d. As shown in Fig. 1(b), the spherical tip is an identical, aligned crystal plane bent into a sphere. Tip atoms form a square grid with the same atomic spacing d in the x-y plane, and are displaced in the z direction to lie on the spherical surface. Atoms from opposing surfaces interact with a repulsive Lennard-Jones (LJ) pair potential

$$V_{\rm LJ} = 4\epsilon((\sigma/r)^{12} - (\sigma/r)^6) + \epsilon, \text{for} \quad r < r_c \qquad (1)$$

where r is the atomic separation and ϵ and σ characterize the interaction energy and length scales, respectively. Truncating the LJ potential at its minimum, $r_c = 2^{1/6}\sigma$, and shifting the potential to zero at this radius ensures the potential is purely repulsive. In the following, the length scale of interactions inside the substrate and across the interface are assumed to be approximately equal so that $d = r_c = 2^{1/6}\sigma$. The main effects of changes in σ/d are discussed below.

The elastic response of substrate atoms is calculated using an efficient Green's function (GF) method.[19,20] This accelerates atomistic simulations of crystalline solids by using linear response in regions where strains are small. For elastic interactions within the crystal, we use the GF for a continuous, semi-infinite, isotropic solid. To map atomic forces onto this continuum description, we use a homogeneous pressure on square patches of area d^2. The discrete Green's function is obtained from a triangulation of these patches and the analytical solution for loaded triangles.[28] This allows direct comparison to past continuum theories and simulations[14,18,21] and we found similar results for anisotropic crystalline lattices. A square region with L atoms per edge is treated explicitly. Contact is limited to the central region of size $L/2$ and a padding method is used to reproduce the response of a semi-infinite solid.[29,30]

The Poisson ratio is set to $\nu = 0.5$ to decouple normal and horizontal displacements[2] and thus ensure that the substrate and sphere remain commensurate during normal loading. Following Hurtado and Kim, the stiffness of the solid is characterized by the shear modulus G. This is related to the Young's modulus E and indentation modulus $E^* \equiv E/(1-\nu^2)$ by $G = E/3 = E^*/4$.

In experiments, tips typically advance at much lower velocities than simulations can access. To model quasi-

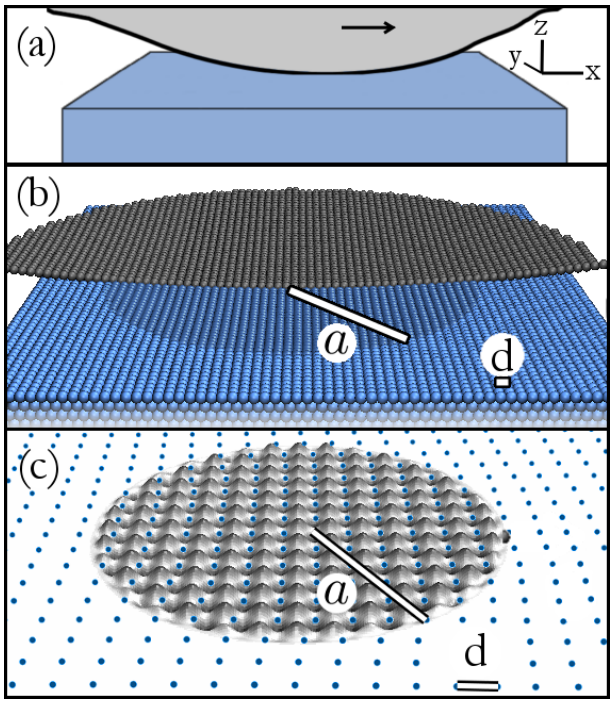

FIG. 1: (a) We consider an idealized spherical tip sliding on a flat elastic substrate with no adhesive interactions. Motion is in the x-direction and the substrate surface is normal to the z-axis. In the continuum picture the surfaces are smooth on scales less than the sphere radius R. (b) Explict MD simulations include atomic surface structure (Sec. IIA). A bent, commensurate crystalline lattice most closely mimics the continuum picture. In the image, much of the rigid sphere has been cut away to show the substrate atoms that experience a repulsive force (in darker color)and are displaced downwards to form a curved indentation. (c) In the lateral force model (Sec. IIB), shear forces are applied directly to the substrate atoms with a peak shear stress proportional to the local pressure predicted by Hertz theory. There is no normal force on the substrate and it remains flat. Ref. 21 used the same geometry but with a constant maximum shear stress to model adhesive contacts.

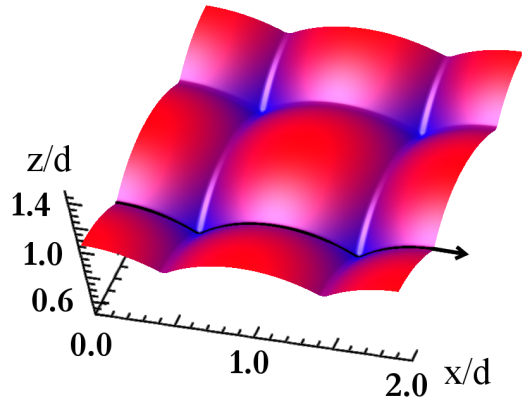

FIG. 2: Variation of the height of an atom as it moves over a rigid substrate at a fixed normal force of $1.0\epsilon/\sigma$. The height is periodic in the atomic spacing $d = 2^{1/6}\sigma$ and the black line indicates the minimum energy path between successive minima. The lateral force is equal to the slope along this path times the normal force and the local static friction coefficient α equals the maximum slope along this path.

static motion, the tip is displaced in small increments and the resulting atomic displacements are determined by energy minimization.[31] First, normal tip displacements are applied to achieve the desired normal load. Then the lateral friction force is measured as a function of lateral displacement by making steps of $0.01d$ at fixed load. The energy minimization tolerance on the global force vector norm was less than $10^{-6}\epsilon/d$ per atom in the contact. Tests showed that this tolerance ensured that the system always remained in the local energy minimum. We present results for R/d from ~ 270 to 41000, corresponding to ~ 100nm to 12μm.

The repulsive LJ interaction between commensurate surfaces (Eq. 1) produces a local friction that follows Amontons' law, i.e. the friction force is proportional to the local normal force.[32] This is because the stiff LJ potential acts like a hard wall, effectively creating microscopic ramps encountered by each atom along its sliding path. Figure 2 shows the equilibrium height of a single atom moving over a rigid substrate at a fixed normal force of $1\epsilon/\sigma$. As for sliding on an inclined plane, the lateral force needed to move the atom is just the normal force times the slope of this surface. The static friction coefficient is the maximum slope along the sliding path (black line in Fig. 2). The LJ repulsion rises so rapidly with decreasing separation that the slope of the sliding path varies little with the magnitude of the normal force. Thus the static friction for a single atom has a nearly load independent coefficient of friction $\alpha = 0.7$. As discussed previously,[25,33] α is most sensitive to changes in σ/d. Decreasing σ/d allows the atom to penetrate more deeply between substrate atoms and thus increase the slope of the sliding path and the value of α.

B. Lateral Force Model (LFM)

In a spherical contact, there is a spatially varying normal force on atoms that is approximately described by Hertz theory.[34–36] This leads to a spatially varying friction force on atoms. However the total friction coefficient for a rigid spherical tip is equal to the local friction coefficient α because all atoms advance in registry. The friction coefficient can change if substrate elasticity allows atoms to advance independently.[14,15,18,21] The elastic response also produces changes in the slope and curvature of the substrate. To remove any influence of these changes we considered a simpler model where the surface remains flat. This lateral force model also allows the effect of changes in σ/d and α to be explored.

In the lateral force model, the spherical tip is replaced by a lateral force field that only depends on the position of substrate atoms in the $x-y$ plane (Fig. 1(c)). There are no normal forces or displacements. In a recent paper we considered the case of adhesive interactions where the lateral force was independent of normal load.[21] Here we modify the potential so it mimics the friction under the explicit spherical tip where the normal force varies within the contact but the local friction coefficient is constant.

To capture the periodic variations in force at the atomic scale (Fig. 2), we use a simple sinusoidal force like that used for the Frenkel-Kontorova chain and the two-dimensional Peierls-Nabarro model.[18,37] Pressure variations on the scale of the contact radius are included by varying the magnitude of the sine wave with the distance r from the tip center. The force applied to an atom at position (x, y) relative to the tip center is

$$\boldsymbol{f}(x,y) = \tau_{\max}(r) d^2 \left[\hat{\boldsymbol{x}} \ \sin\left(\frac{2\pi x}{d}\right) + \hat{\boldsymbol{y}} \ \sin\left(\frac{2\pi y}{d}\right) \right]. \tag{2}$$

Here, $\tau_{\max}(r)$ is an envelope function that gives the magnitude of the maximum local frictional stress and goes to zero outside the contact, $r > a$. In the explicit simulations there is a constant local friction coefficient α and the local normal force is approximately consistent with the profile predicted by Hertz theory. We thus set

$$\tau_{\max}(r) = \alpha p_0 \sqrt{1-(r/a)^2} \quad , \tag{3}$$

where p_0 is the Hertz prediction for the pressure in the center of the contact and the factor of d^2 in Eq. 2 converts this to a force per atom. For a normal load F_z, $p_0 = 3F_z/2\pi a^2$ and $a^3 = 3F_z R/4E^*$.

Note that the tip radius R enters p_0 even though there is no explicit curvature in the lateral force model. Increasing the tip radius lowers the load required to achieve a given contact radius and thus lowers the local pressure,

$$p_0 = \frac{2a}{\pi R} E^* = \frac{3F_z}{2\pi a^2} \quad . \tag{4}$$

Thus the lateral force model captures changes in contact forces in the explicit model without introducing vertical surface distortions that are often ignored in continuum theory.[2] These effects limit us to $a/R < 0.1$ in the explicit model but not in the lateral force model.

The local friction coefficient α enters as a multiplicative factor of p_0 in Eq. 3 so the lateral force model for a given a only depends on α/R and not on α or R independently. Results for μ/α at a given R can be mapped to those for a different local friction coefficient with the radius scaled by the same factor. In the results section we quote values of R corresponding to the same $\alpha = 0.7$ as the explicit model, but the collapse of data for different R also provides a test of the scaling with α.

One important difference between the explicit and lateral force models is the shape of the local potential. The lateral force model is a simple sine wave, while the LJ potential gives very sharp changes in slope near the minima (Fig. 2). Despite this qualitative difference, we find that the two models give nearly the same behavior. This is a powerful confirmation that atomistic details only enter through α and d.

In both models the component of the shear stress in the y-direction is less than 1% except in special cases, such as near the cores of defects where it may be of order 5%. As a result we only report local and total stresses along the sliding direction x and τ will refer to the stress in that direction.

Just as for the explicit model, quasi-static sliding is simulated by iteratively translating the tip center relative to the bottom of the substrate. After each step of $0.01d$ in the $+x$-direction the energy is minimized as in the explicit model. Minimization can be very slow for large contacts when changes are dominated by dislocation motion along the interface. Assuming $\alpha = 0.7$, the effective sphere radii studied with the lateral force model span from 10 to $10^4 d$.

III. RESULTS

As in the case of adhesive contacts,[14,15,18,21] we observe three regimes of frictional sliding as the contact area increases. However the scaling behavior is different because the local friction is proportional to normal load instead of area. We give a brief overview of the regimes and then analyze each in detail in a separate section.

In Regime I, characteristic of small contacts, there is no appreciable elastic deformation on the length scale of the contact during sliding. As illustrated in Fig. 3(a), substrate atoms hop coherently past atoms on the rigid tip, and the coefficient of friction equals the local value, $\mu = \alpha$. In larger contacts, elastic deformation occurs and slip is mediated by the nucleation of a lattice dislocation that rapidly moves across the interface. This is Regime II and is illustrated in Fig. 3(b). In Regime III, the contact is large enough that many dislocations are arrested at the interface. The static friction is set by the condition for dislocations to unpin and move along the interface (Fig. 3(c)).

Hurtado and Kim discussed these three regimes for adhesive contact and used analytic arguments to identify the scaling behavior in Regime II. Later work[18,21] showed that the key length scale is the characterisitic core width of interfacial edge dislocations:

$$b_{\text{core}} \equiv d \frac{G}{\tau_{\max}} \tag{5}$$

where $\tau_{\max}$ is the maximum lateral stress between surfaces. For adhesive contact models $\tau_{\max}$ is assumed to be independent of load. In contrast, the peak lateral stress is proportional to the local pressure for the repulsive contacts considered here. As a result, the core width varies across the contact and diverges at the edge of the contact. This variation is key to the different scaling behavior for repulsive contacts that we describe below.

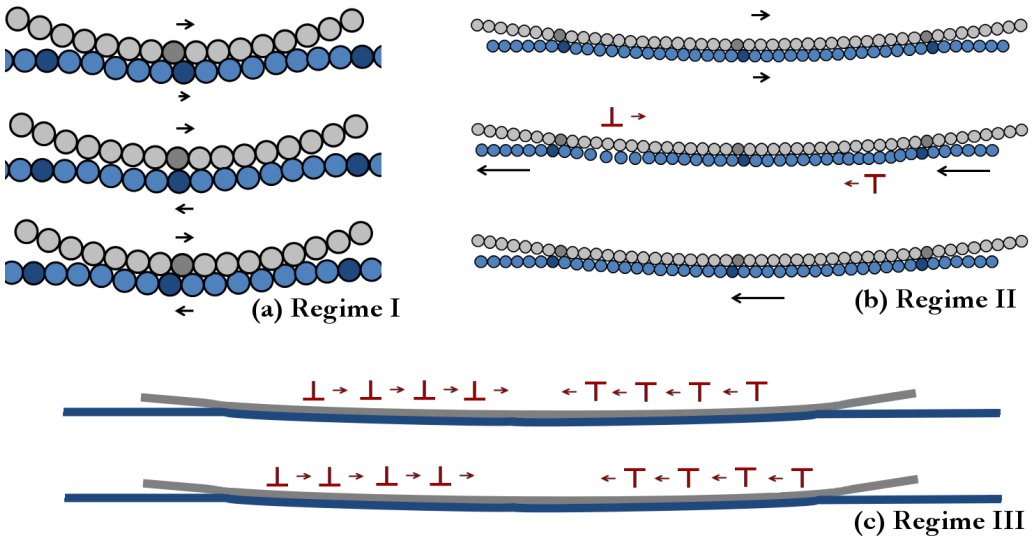

FIG. 3: Schematic of (a) rigid slip (Regime I), (b) slip by dislocation nucleation (Regime II), and (c) slip by dislocation unpinning (Regime III). Pictures show cross-sections along the sliding direction x at different displacements, with the top snapshot corresponding to the maximum friction. Some atoms are labeled with darker colors to show relative motion. In (a), the rigid asperity slides over the substrate and any lateral displacements in the substrate are too small to alter the registry of atoms on opposing surfaces as the relative position of the tip increases by d from the first to third snapshot. In (b), atoms in the top snapshot are pinned but a small displacement leads to the second snapshot where a dislocation loop nucleates near the edges of the contact. The dislocation has Burgers vector $\boldsymbol{b} = d\hat{x}$ and line tangent $\hat{\xi} = \hat{y}$ into the page at the front of the contact (upside down T) and $\hat{\xi} = -\hat{y}$ at the back of the contact (T). The dislocation glides through the contact and self-annihilates, resulting in slip by a Burgers vector. In (c) the contact is so large that many dislocations become arrested in the contact and further sliding of the asperity is required for them to self-annihilate.

We define a dimensionless parameter related to the ratio of contact radius to the minimum core width, $b^0_{\rm core}$, which occurs in the center of the contact. Using the Hertz prediction for pressure (Eq. 4),

$$\frac{a}{b^0_{\rm core}} = c\frac{\alpha a^2}{Rd} \tag{6}$$

where for general ν the ratio of G to E^* gives $c = 4/(\pi(1-\nu))$ and $c = 8/\pi$ for $\nu = 0.5$. Note that, as in the lateral force model, the local friction coefficient and radius only enter as α/R. When $a/b^0_{\rm core}$ is small, a dislocation can not fit in the contact and the atoms should advance coherently as in Regime I. Regime II should set in for $a/b^0_{\rm core} > 1$.

Figure 4 shows that the ratio defined in Eq. 6 is the relevant parameter for Regimes I and II. For a given simulation we define the coefficient of static friction μ as the ratio of the maximum lateral force to the load. All results for μ/α in the explicit model and lateral force model at different sphere radii collapse onto a universal curve until they reach Regime III. Regime I corresponds to $a/b^0_{\rm core} \ll 1$ and $\mu/\alpha \approx 1$. In Regime II, $a/b^0_{\rm core} \gg 1$ and the friction coefficient drops as a power of contact radius. The crossover between the two regimes occurs over a broad range near $a/b_{\rm core} = 1$ with noticeable suppression of μ well below unity and the assymptotic power law scaling reached by $a/b_{\rm core} = 10$. The success of the collapse in this figure shows that the lateral force model captures the essential physics of the explicit model and thus that curvature of the substrate and the shape of the local periodic potential are not important. The following sections analyze each of the three regimes in detail.

A. Regime I

In Regime I, all atoms advance coherently. From the Peierls-Nabarro model of dislocations,[16] $b_{\rm core}$ is the shortest length scale over which the interfacial corrugation is strong enough to strain the crystal so that the registry changes by the Burgers vector d. If a contact has radius $a < b_{\rm core}$, the lateral displacement of atoms differs by less than d and their contributions to the lateral force add in phase. Since the core width is smallest in the center of a repulsive contact, Regime I corresponds to $a < b^0_{\rm core}$.

As the lateral displacement of the tip increases, the lateral force on each atom rises. All reach the maximum local lateral force at the same time. Since the maximum lateral force is just α times the local normal force, summing over the contact gives a total static friction $F_s = \alpha F_z$. Thus the entire contact obeys Amontons' law with a coefficient of friction equal to the local value α. Figure 4 shows that μ/α is unity for small $a/b^0_{\rm core}$ and has dropped by about 20% at $a/b^0_{\rm core} = 1$

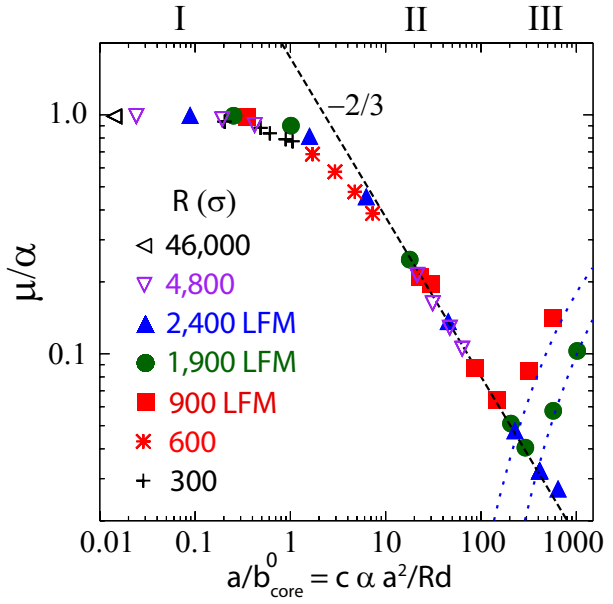

FIG. 4: Static friction coefficient for non-adhesive surfaces plotted against the ratio of the contact radius a to the dislocation core width $b^0_{\rm core}$ in the center of the contact (Eq. 6). Results are shown for the explicit atomistic model (open triangles, asterixes and pluses) and lateral force model (closed triangle, circle and square) as a increases at the indicated sphere radius ($\sigma = 2^{-1/6}d$). The lateral force model only depends on α/R, and values of R in the legend correspond to the same $\alpha = 0.7$ as the explicit model. The three regimes of different sliding mechanism are indicated at the top of the figure. The friction is constant in Regime I, drops as a power law in Regime II and rises in Regime III. A black dashed line shows the power law of -2/3 expected in Regime II. Blue dotted lines show the predictions for Regime III.

Another type of elastic deformation could be relevant in Regime I. Even though contacting atoms move coherently, substrate elasticity leads to an average lateral displacement δ relative to the bottom of the substrate that rises with the lateral force F. From continuum theory the average stiffness is:

$$k \equiv F/\delta = 8Ga/(2-\nu) \quad . \tag{7}$$

If this stiffness is too low, the contact may advance in a discontinuous series of sticks and slips.

Since all the atoms advance coherently, the lateral force model for the contact in Regime I is a realization of the single-particle Prandtl-Tomlinson (PT) model.[18,26] The PT model considers a single particle pulled by a spring of stiffness k through a sinusoidal potential with period d and maximum force F_s. The dimensionless constant

$$\lambda \equiv 2\pi F_s/dk \tag{8}$$

characterizes the ratio of interfacial stiffness to elastic stiffness. The particle advances smoothly when $\lambda < 1$ and stick-slip motion occurs for larger λ.[26] Given the definition of λ, the transition corresponds to the point where the mean lateral displacement at the static friction force is $d/2\pi$.

We can calculate λ in Regime I using $F_s = \alpha F_z$ and the Hertz relation between a and F_z. This yields

$$\lambda = \frac{\pi(2-\nu)E^*}{3G}\frac{\alpha a^2}{dR} = \frac{\pi^2}{4}\frac{a}{b^0_{\rm core}} \tag{9}$$

Thus as long as the system is well within Regime I, one has $\lambda < 1$, and the contact will advance smoothly.

The solid line in Figure 5 shows a typical force trace for the lateral force model in Regime I. Because the substrate is very stiff ($\lambda < 1$), there is little lateral displacement of substrate atoms as the tip displacement Δx increases. The lateral force has the sinusoidal form of the interfacial interaction for each atom in Eq. 2. For the explicit model we also find that the lateral force in Regime I has the same form as the force per atom, in this case the slope of the surface in Fig. 2. Stick-slip will only occur in Regime I if an additional compliance is inserted, such as a soft atomic force microscope cantilever.[26,38,39]

Note that positive and negative values of the friction are sampled almost equally in the friction trace for Regime I ($a/b^0_{\rm core} \ll 1$). Thus the kinetic friction obtained by time-averaging the force is nearly zero even though the static coefficient of friction has its maximum possible value, $\mu = \alpha$. This strong contrast between kinetic and static friction is common for systems that move smoothly without stick-slip or other internal elastic instabilities at the interface.[26] Such instabilities play an important role in Regimes II and III.

B. Regime II

1. *Friction Versus Displacement*

In Regime II, the tip advances in steps as dislocations nucleate and sweep across the contact. Typical results for the friction curves are shown as dashed and dotted lines in Fig. 5. The total force (Fig. 5) grows linearly at first, with a slope that approaches the continuum prediction for the stiffness k (Eq. 7) as $a/b^0_{\rm core}$ increases. A dislocation nucleates at the force maximum corresponding to the static friction and then the force drops rapidly as the dislocation moves to the center and annihilates, advancing the tip by about d. This cycle repeats as the tip advances, yielding a classic stick-slip force trace.

As $a/b^0_{\rm core}$ increases, the static friction coefficient μ decreases. At the same time, the fraction by which the force drops during slip decreases. This means that the time-averaged force, corresponding to the kinetic friction, approaches the static friction μ. By $a/b^0_{\rm core} = 6$ the kinetic friction is already about 2/3 of the static friction.

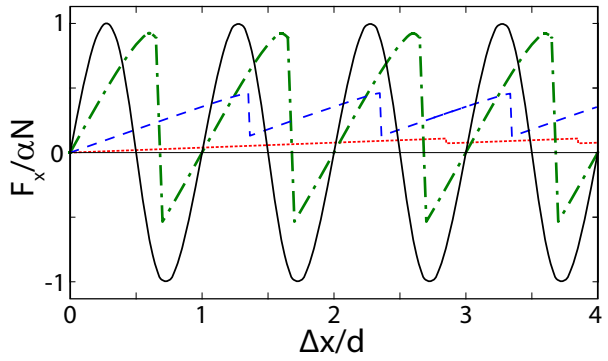

FIG. 5: Friction normalized by maximum static friction αN as a function of lateral tip displacement Δx normalized by nearest-neighbor spacing d for the lateral force model with $R = 535d$ and different values of $a/b^0_{\rm core}$: 0.054 (solid line, $a/d = 4$), 1 (dash-dotted line, $a/d = 16$), 6 (dashed line, $a/d = 43$) and 64 (dotted line, $a/d = 138$). In Regime I (solid line), atoms move in phase and the total lateral force is proportional to the periodic force on each atom (Eq. 2). The static friction coefficient $\mu = \alpha$ and the kinetic friction, corresponding to the time-average force, is nearly zero. At $a/b^0_{\rm core} = 1$, the static friction is depressed, sharp drops are becoming evident and the kinetic friction has increased to about a third of the static friction. In Regime II (dashed and dotted lines), the tip begins to advance in discrete stick-slip events associated with dislocation motion. The kinetic friction approaches the static friction, while μ drops with increasing $a/b^0_{\rm core}$.

2. *Local Stress*

Fig. 6 shows the local shear stress at points along the sliding (x) and transverse (y) axes for the lateral force model with $a/b^0_{\rm core} = 6.23$. Dashed lines in Fig. 6 show the maximum local shear stress, which is just α times the normal pressure from Hertz theory (Eq. 3). The actual local shear stress must always be below this value. As the lateral displacement of the tip rises, τ grows throughout the contact. The black squares in Fig. 6 show the stress τ^b before dislocation nucleation at the force maximum corresponding to the static friction. After the dislocation sweeps across the interface, the stress drops to the curve labelled τ^a in Fig. 6.

To understand the plots described above and the scaling of nucleation with contact size we use the well-known continuum elastic solutions for circular contacts.[2] If the contact advances uniformly with the tip so there is no relative displacement between tip and substrate atoms, the lateral stress is lowest in the center and diverges inversely with the square root of the distance from the edge of the contact:

$$\tau(r) = \frac{F_x}{2\pi a^2}\left[1-(r/a)^2\right]^{-1/2} \qquad (10)$$

As in the case of a crack tip, this singularity is caused by a discontinuity in boundary condition from constant displacement inside the contact to zero stress outside. In any physical system, the singularity is cut off at small scales by atomic discreteness or by deviations from the assumption of uniform displacement. Cattaneo-Mindlin (CM) theory assumes the singularity is removed by slip between tip and substrate in the outer rim of the contact that reduces τ to αp. This local slip leads to a larger tip displacement before sliding than expected from Eq. 7, but the CM model predicts sliding of the whole tip starts when $\mu = \alpha p$ throughout the contact and thus that there is a scale independent static friction coefficient $\mu = \alpha$.

The solid line in Fig. 6 compares the CM prediction for the shear stress to τ^b at the same lateral displacement. Note the differences near the edges of the contact. CM theory predicts zero slip between substrate and tip atoms for $|r| \lesssim 0.8a$. Analysis of atomic configurations in our simulations shows that the relative displacement of substrate and tip atoms is nonzero throughout the contact. Indeed the lateral stress results from a relative displacement in the periodic potential of Eq. 2. The nearly constant τ^b in the central region means that there is a nearly constant relative displacement. The displacement increases as τ^b rises near the edges of the contact. However τ^b cannot rise above the maximum value that corresponds to a displacement of $d/4$, and any further displacement lowers $\tau/\tau_{\rm max}$. Along the sliding direction (Fig. 6(a)), τ remains close to $\tau_{\rm max}$ out to the edge of the contact. Along the perpendicular axis (Fig. 6(b)), the displacement continues to grow, causing $\tau^b/\tau_{\rm max}$ to drop and even become negative.

The periodicity of the potential introduces a minimum change in displacement $\sim d$ for τ to return to $\tau_{\rm max}$. Since the displacement can only change by d over a lateral distance $b_{\rm core}$, the stress must change from maximum to negative to maximum over a distance $b_{\rm core}$. Neither d nor $b_{\rm core}$ are included in the CM model, which assumes any infinitesimal displacement is able to change τ to $\tau_{\rm max}$. As a result, the CM model predicts a singularity in the derivative of the lateral displacement of substrate atoms and a cusp in the predicted shear stress. In an atomistic system, the cusp is broadened over the local core width. Eq. 5 gives the core width for an edge dislocation which is $a/6.23$ at the center of the contact. This is comparable to the range where τ^b deviates from the CM prediction in Fig. 6(a). Similar behavior is observed throughout Regime II, but as $a/b^0_{\rm core}$ increases the range over which there is a deviation from the CM prediction becomes narrow and harder to observe in plots.

The breaking of radial symmetry in Fig. 6 is not expected from continuum theory.[2,14] A uniformly-displaced circular contact leads to a radially-symmetric stress in a linear isotropic solid, and Cattaneo-Mindlin theory retains this symmetry. Our results are also nearly symmetric at small tip displacements, but asymmetry becomes pronounced near the static friction. As seen in Fig. 6, τ^b rises more rapidly along y than along x and reaches a higher maximum at a smaller radius. After the maximum, the ratio $\tau^b/\alpha p$, and thus the displacement of

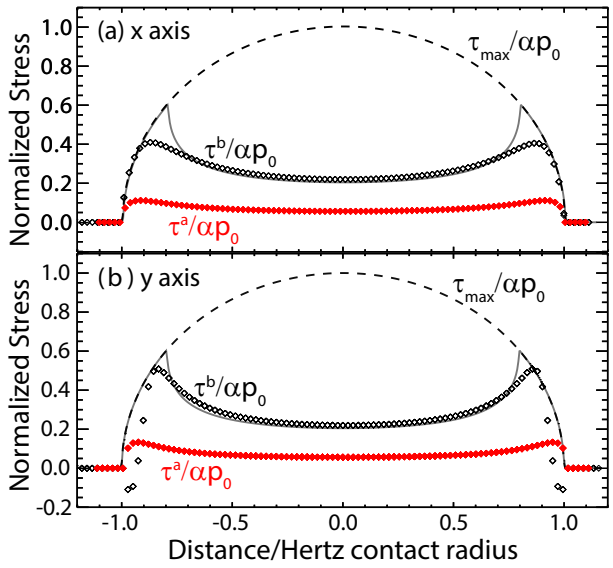

FIG. 6: Variation in shear stress for points along the (a) x-axis (sliding direction) and (b) y-axis (transverse direction) in the lateral force model. Diamonds show the shear stress τ^b (black, open) just before dislocation nucleation ($\Delta x/d = 1.35$ in Fig. 5), and just after nucleation and annihilation, τ^a (red, closed). A dashed line shows the maximum local shear stress $\tau_{\max}$, which is α times the Hertz prediction for the local pressure. Stresses are normalized by the peak value at the origin, αp_0, and distances by the Hertz prediction for the contact radius. The solid line shows the Cattaneo-Mindlin prediction for the shear stress. Here $a = 43d$, $R = 535d$, and $\alpha = 0.7$. This corresponds to $F_z = 806Gd^2$, $b^0_{\rm core} = 6.9d$ and $a/b^0_{\rm core} = 6.23$.

atoms relative to the tip, changes more rapidly along y than along x. All of these results indicate that the effective dislocation core width is smaller along the transverse y-axis.

The negative values of stress for $|y|$ near the edge of the contact signal the onset of an instability. An increase in tip displacement causes atoms to jump by d to create a dislocation with Burger's vector $d\hat{x}$ along the sliding direction. Along the sides of the contact ($|y| \approx a$), this corresponds to a screw dislocation (Burger's vector along dislocation line) while at the front and back of the contact it is an edge dislocation (Burger's vector perpendicular to the dislocation line). Screw dislocations typically have lower physical core widths than edge dislocations.[16] This explains the faster variations of τ^b along y. The smaller core width leads to less smoothing of the cusp predicted by CM theory and a higher stress. These changes cause dislocations to nucleate first along the y-axis. A similar phenomenon is observed in sliding of elastomer spheres on a hard substrate.[40]

The asymmetric nucleation of dislocations is illustrated in Fig. 7 for contacts in Regimes II and III where dislocations do not annihilate immediately. Screw-character dislocations nucleate at the top and bottom of the contact. They move toward the center with increasing tip displacement until edge-character dislocation segments nucleate at the front and back of the contact, resulting in an oval dislocation loop (Fig. 7(a)). In Regime II, a single unstable loop forms and continues to shrink until it annihilates in the center of the contact. The tip has then advanced by about d leading to a slip in the force trace (Fig. 5). Near the transition between Regime II and III, one or two dislocation loops can be stably pinned in the contact (Fig. 7(a,b)). For the adhesive model studied previously the core width and Peierls stress are independent of radius and the dislocation loop is strongly affected by lattice anisotropy and dislocation character (Fig. 7(c)). For the repulsive model considered here, the strong variation of core width with pressure leads to more circular dislocation loops (Fig. 7(a,b)).

The explicit model shows qualitatively similar behavior to the lateral force model, but curvature and atomic height variations lead to further complexity. Fig. 8 shows the shear and normal stress in a contact with the same normal force and sphere radius used in Fig. 6. As before, shear stresses are normalized by αp_0 where p_0 is the Hertz prediction and distances are normalized by the Hertz contact radius. In the lateral force model a is equal to the Hertz prediction by construction, but atomistic effects lead to small deviations in the explicit model.[35,36] The distribution τ^b is obtained just before a dislocation nucleates and τ^a is the stress just after a nucleation sweeps through the interface. The corresponding normal pressures p^b and p^a are also shown. With the same normalization, the maximum local shear stress $\alpha p/\alpha p_0 = p/p_0$.

As shown in earlier work,[35,36] at low lateral forces the pressure is close to the Hertz prediction. The finite range of interactions and roughness associated with atomic structure smear the pressure at the edge of the contact and p goes to zero about $2d$ outside the Hertz prediction for a. At higher lateral forces, a kink develops in the local pressure. Changes in lateral displacement between tip and substrate atoms lead to vertical displacements, because atoms move up the ramps illustrated in Fig. 2. The peak in the shear stress is at the maximum slope of the sliding path. The maximum height is past this point, leading to smaller spacings from tip atoms and a pressure bump in this outer region. The changes are more pronounced for the y-axis and dislocations nucleate at the sides of the contact not the front and back.

Another clear difference from the lateral force model is the asymmetry between the front and back of the contact in the explicit model. The curvature of the spherical asperity leads to a change in surface slope that is not included in continuum theory or the lateral force model. The shear force τ is taken from the x component of the force in Fig. 8, but the local normal and lateral directions of the sphere surface rotate with the local slope. There are higher values of F_x at the front of the sphere where the local normal force resists sliding and lower values of F_x at the back of the sphere where the slope assists sliding.

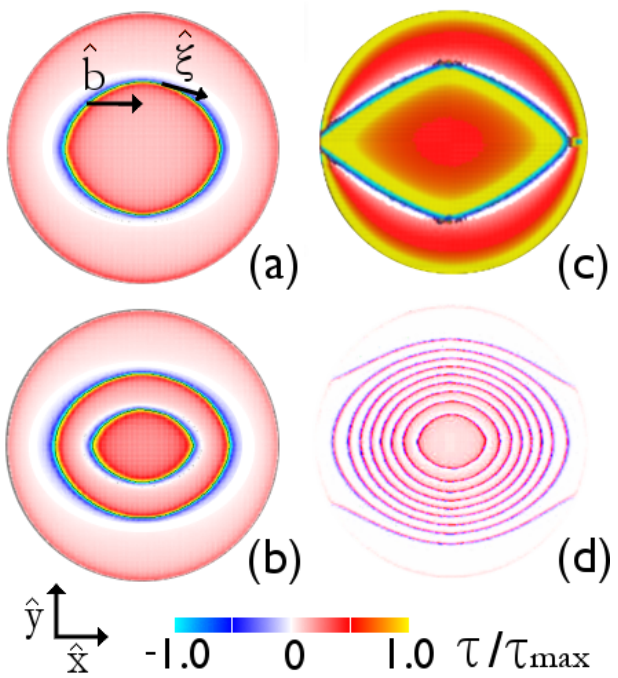

FIG. 7: Snapshots showing local shear stress relative to the local maximum shear stress using the color map indicated by the bar at the bottom of the figure. Dislocations are located in regions where stress changes sign over the core width. Each has Burgers vector $\vec{b} = d\hat{x}$ along the sliding direction and the local orientation $\hat{\xi}$ varies around the loop. Panels (a) and (b) show the lateral force model near the crossover from Regime II to Regime III ($a/d = 126$ and $a/b^0_{\rm core} = 70$). Panel (a) shows the first dislocation that forms, (b) shows a state just before sliding where a second dislocation has formed. After a small additional displacement the second dislocation annihilates, and the system returns to the configuration of panel (a). Panel (c) shows an example of the anisotropic dislocation loops that form in the adhesive model of Ref. 21 with $a/b_{\rm core} = 126$ and $b_{\rm core} = d$. Panel (d) shows a case from Regime III of the lateral force model ($a/d = 510$ and $a/b^0_{\rm core} = 278$). Two dislocation lines with predominantly screw character (nearly horizontal so that $\hat{\xi} \parallel \hat{b}$) have nucleated near the top and bottom of the contact and terminate at the contact edge. As dislocation lines move into the center, they develop into closed loops.

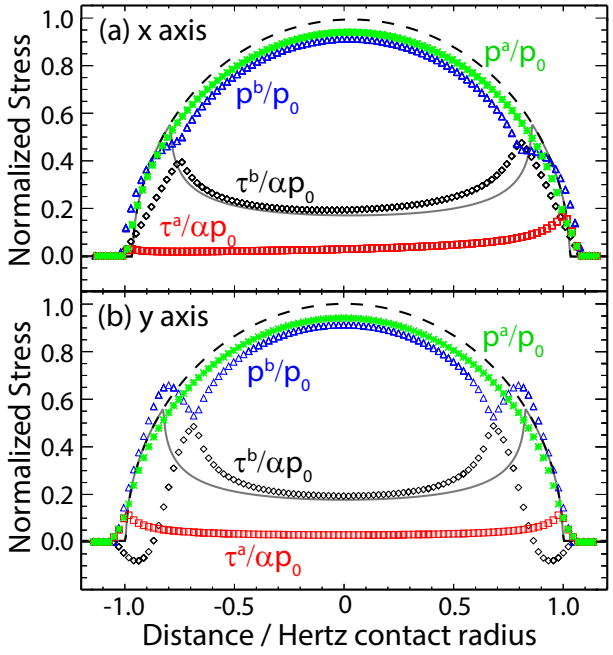

FIG. 8: Variation in stress across the contact for atoms along the (a) x-axis (sliding direction) and (b) y-axis (transverse direction) for the explicit model. Diamonds show the shear stress τ^b just before dislocation nucleation, and squares show the stress τ^a just after nucleation and annihilation. Also shown is the local maximum shear stress αp before and after nucleation, where p^b (triangles) and p^a (asterixes) are measured locally from the force on an atom divided by the atomic area d^2. Lines give the Hertz prediction for αp (dashed) and CM prediction for τ (solid). The Hertz prediction for contact radius and αp_0 are used to normalize position and stress, respectively. As in Fig. 6, $F_z = 806Gd^2$ and $R = 535d$. The static friction is measured to be $F_x = 222Gd^2$, and $\mu = 0.28$.

In regions where the interfacial stress from Eq. 2 decreases with increasing displacement, an individual atom is linearly unstable against a forward jump. Substrate atoms near the edge of Fig. 6(b) are in this region where stress drops and would jump by $\sim d$ relative to the tip if they where not held back by elastic interactions with their neighbors. When the width of the unstable rim is approximately the local $b_{\rm core}$, atoms in this region can all advance by a lattice constant to create a dislocation. The lateral force at the onset of nucleation is the static friction and drops farther below α as $a/b_{\rm core}$ increases. A scaling relation is derived in the next subsection.

3. *Scaling of μ With Contact Size*

Rice has presented an analysis of dislocation nucleation along a crystalline plane.[41] Hurtado and Kim applied this analysis to the case of a circular contact with consant maximum shear stress $\tau_{\rm max}$.[14] Nucleation occurs[18,21] when the shear stress reaches $\tau_{\rm max}$ at a distance $c_0 b_{\rm core}$ from the contact edge where c_0 is a constant. Because both $\tau_{\rm max}$ and $b_{\rm core}$ are constant, the analysis gives a friction stress $\tau_{\rm fric} \sim a^{-1/2}$ in Regime II, where the exponent 1/2 reflects the power law singularity in shear stress.[18] For the repulsive case considered here, the variation in maximum shear stress with pressure must be included, and $b_{\rm core} \to \infty$ near the contact edge. This changes the power law relating friction and contact radius.

To incorporate the variation in core width with radius we calculate the relevant value, $b^*_{\rm core}$, self-consistently. In particular we find the condition for the shear stress at a distance $c_0 b^*_{\rm core}$ from the edge of the contact to be equal to $\tau^*_{\rm max}$, the maximum shear stress associated with the normal pressure at the same distance.

Far from Regime I, nucleation occurs near the edge of the contact where the stress singularity dominates. Assuming $c_0 b^*_{\rm core} \ll a$, the stress at a distance $c_0 b^*_{\rm core}$ from the edge of the contact is dominated by the stress singularity. Using the analytic form for the stress in Eq. 10,

$$\tau^* = \frac{F_x}{2\pi a^2}\left[1-\frac{(a-c_0 b^*_{\rm core})^2}{a^2}\right]^{-\frac{1}{2}} \approx \frac{F_x}{2\pi a^2}\left[\frac{2c_0 b^*_{\rm core}}{a}\right]^{-1/2}$$

where F_x is the total lateral force.[2] One obtains Hurtado and Kim's result that $F_x/\pi a^2 \sim a^{-1/2}$ by equating τ^* to the constant $\tau_{\rm max}$ assumed for adhesive contacts:

$$\frac{F_x}{\pi a^2 \tau_{\rm max}} = 2\left[\frac{a}{2c_0 b_{\rm core}}\right]^{-1/2}. \qquad (11)$$

Our previous numerical fits[21] would correspond to $c_0 = 0.18$.

For the repulsive contacts considered here, we use the Hertzian pressure distribution to determine αp at a distance $c_0 b^*_{\rm core}$ from the edge. Expanding Eq. 3 for $b^*_{\rm core} \ll a$ and using Eq. 4 for F_z, we find

$$\tau^*_{\rm max} = \alpha p_0\left[1-\frac{(a-c_0 b^*_{\rm core})^2}{a^2}\right]^{1/2} \approx \frac{3\alpha F_z}{2\pi a^2}\left[\frac{2c_0 b^*_{\rm core}}{a}\right]^{1/2} \qquad (12)$$

Equating this to τ^* yields a prediction for the static friction coefficient:

$$\mu = F_x/F_z = 6c_0\alpha b^*_{\rm core}/a. \qquad (13)$$

We can rewrite the expression for μ in terms of $a/b^0_{\rm core}$ using Eq. 12 and the general relation between $b_{\rm core}$ and $\tau_{\rm max}$ from Eq. 5. Multiplying Eq. 12 by a/dG to convert the stresses to core widths we find

$$\frac{a}{b^*_{\rm core}} = \frac{a}{b^0_{\rm core}}\left[\frac{2c_0 b^*_{\rm core}}{a}\right]^{1/2}, \qquad (14)$$

and thus

$$\frac{2c_0 b^*_{\rm core}}{a} = \left[\frac{2c_0 b^0_{\rm core}}{a}\right]^{2/3} = \left[\frac{2c_0 dR}{c\alpha a^2}\right]^{2/3}, \qquad (15)$$

where the last relation follows from Eq. 6. The friction coefficient is readily obtained by substituting this expression into Eq. 13. Normalizing by the local friction coefficient α we find:

$$\frac{\mu}{\alpha} = 3\left[\frac{2c_0 b^0_{\rm core}}{a}\right]^{2/3} = 3(2c_0)^{2/3}\left[\frac{c\alpha a^2}{dR}\right]^{-2/3}. \qquad (16)$$

All of our results for the lateral force and explicit model in Regime II (Fig. 4) are consistent with the power law scaling predicted by Eq. 16. The fit line corresponds to $c_0 = 0.22$, which is comparable to the value of $c_0 = 0.18$ obtained for an adhesive model in Reference 21. Experimental results are typically plotted vs. load since a is difficult to measure. Since a rises as the 1/3 power of the load, we find

$$\frac{\mu}{\alpha} \sim F_z^{-4/9}. \qquad (17)$$

C. Regime III

1. *Spatial Distribution of Stress and Dislocations*

In Regime III, a dislocation is nucleated at the contact edge and starts to move towards the center of the contact where the stress is lower. At some radius, the shear stress drops below the Peierls stress $\tau_{\rm Peierls}$ needed to move the dislocation and it becomes arrested in the contact. Additional lateral displacement of the tip raises the local stress above $\tau_{\rm Peierls}$ and depins the dislocation. New dislocations are also nucleated at the edge of the contact and move inward to create a growing array of dislocations. The ultimate static friction is determined by the stress needed to move this array of dislocations towards the center where they annihilate. Because there are a large number of dislocations, the friction remains very close to the static friction and the kinetic friction is nearly equal to the static friction.

Fig. 7(d) shows a snapshot of the dislocation array just before sliding for a system in Regime III. In the case shown, there are eight fully-formed dislocation loops arrested in the contact. The higher energy of edge dislocations[16] means that dislocation loops tend to minimize that character, leading to an oval shape that is elongated in the x-direction. There are also two screw dislocations that have nucleated at the top and bottom of the contact and are moving inward before forming a complete loop. The total number of loops increases with $a/b_{\rm core}$ and the precise pattern results from dislocation interactions as well as variations in core energy and Peierls stress with radius and dislocation character (orientation), as discussed below.

Fig. 9 shows plots of the frictional shear stress exerted on the substrate for atoms along the x and y axes of the system shown in Fig. 7(d). In contrast to Fig. 6, there are many stable dislocations in the contact and the plot illustrates how the width of dislocations varies across the contact. The stress is plotted at each atom and the singularity that would occur at the core of each dislocation (vertical blue lines) in the continuum limit is cut off by the finite atomic spacing. On each side of a dislocation, the magnitude of the stress rises rapidly up to the bounds provided by $\pm\tau_{\rm max}$. There is a sharp change in sign at the core center (vertical blue lines). The number of atoms over which the magnitude of the stress rises is proportional to the core width, and is about twice as large along the x-axis as along the y-axis. This is a further illustration that, as shown in Fig. 6 and found in most systems,[16] edge dislocations (perpendicular to x) are wider than screw dislocations (perpendicular to y). The plots also show that the core width of both edge and screw dislocations increases with the distance from the contact center. This is consistent with Eq. 5 and the decrease in local pressure and $\tau_{\rm max}$ near the contact edge.

The shear force for this system changes very little with tip displacement, dropping less than 7% after a static

friction peak. This is because the dislocation array is always nearly unstable. In Fig. 9(a), almost all dislocation cores have atoms near the peak magnitude of the lateral stress (dashed lines). A small increase in stress will cause them to advance. There are a few small advances of individual dislocations and then the central dislocation loop becomes unstable, moves to the center and annihilates. Then the process repeats.

2. Scaling of μ with tip and contact radii

In the classic Peierls-Nabarro model for grain boundaries, the Peierls stress of an edge dislocation falls exponentially with core width.[42] As shown below,

$$\tau_{\rm Peierls} = k_1 \tau_{\rm max} \exp(-k_2 b_{\rm core}/d). \qquad (18)$$

where k_1 and k_2 are constants that depend on dislocation character. In the adhesive model considered in Ref. 21, all the parameters in Eq. 18 are independent of contact radius. Regime III begins when the stress required to nucleate a defect, $\tau_{\rm nuc} \propto \tau_{\rm max}\,[a/d]^{-1/2}$, drops to $\tau_{\rm Peierls}$. Since $b_{\rm core}/d = G/\tau_{\rm max}$, the contact radius needed to reach Regime III grows exponentially with increasing substrate stiffness.

For the repulsive model considered here, $\tau_{\rm Peierls}$ changes with radius and load. This leads to different scaling relations. The pressure rises in the center of the contact, leading to an increase in $\tau_{\rm max} = \alpha p$ and a decrease in $b_{\rm core}$ with decreasing distance from the center of the contact. Both effects increase $\tau_{\rm Peierls}$, making it harder to move dislocations in the center of the contact. Using Eq. 6 we find $b^0_{\rm core}/d = R/c\alpha a$ and a central Peierls stress

$$\tau^0_{\rm Peierls} = k_1 \alpha p_0 \exp(-k_2 R/c\alpha a). \qquad (19)$$

To estimate the friction coefficient in Regime III we neglect the variation in $b_{\rm core}$ and assume the local Peierls stress is Eq. 19 with p_0 replaced by the local normal pressure. Then calculating the friction force from the integral over the contact gives

$$\mu/\alpha = k_1 \exp(-k_2 R/c\alpha a). \qquad (20)$$

The actual coefficient will be smaller because of changes in $b_{\rm core}$ that can be included using numerical integration. The transition between Regimes II and III should occur when Eq. 20 and Eq. 16 are equal:

$$\frac{a}{b^0_{\rm core}} = \frac{c\alpha a^2}{dR} \propto \exp(3k_2 R/2c\alpha a). \qquad (21)$$

Thus the crossover to Regime III occurs at a friction coefficient that decreases exponentially with $R/c\alpha a$ and at a contact radius that rises exponentially with this ratio.

One surprising conclusion is that μ increases with load in Regime III. For fixed R, the contact radius rises with load causing the exponential factor in Eq. 20 to rise towards unity. This behavior is clearly shown in the lateral force model results for $R = 1900\sigma$ and 900σ in Fig. 4. The dotted lines are fits using values of k_1 and k_2 obtained below.

We are unable to explore Regime III with the explicit atomistic model because the transition occurs at too large a value of a. To avoid complications from large surfaces slopes at the edge of the contact, the ratio $a/R < 0.1$. Using $\alpha \approx 0.7$ and $c = 8/\pi$ we find that $R/c\alpha a = b^0_{\rm core}/d \gtrsim 6$. This corresponds to $\mu/\alpha \lesssim 0.004$ and $a/d \gtrsim 3 \times 10^4$, which is about an order of magnitude larger than our largest simulations. The lateral force model removes the constraint on a/R because there is no surface curvature. This allows us to explore Regime III and observe the increase in μ with load at large $a/b_{\rm core}$.

3. Peierls Stress for Dislocations

To test Eq. 18 in our system, we performed an independent set of simulations using flat surfaces with periodic boundary conditions. The period $L \geq 256d$ was much larger than $b_{\rm core}$ and the appropriate periodic GF was used.[47] The dislocation was created by using a periodic potential like Eq. 2, but with a small change in period or orientation that frustrates perfect registry between the two surfaces. The potential was chosen so that registry is restored over most of the surface by creation of a single dislocation with Burger's vector $d\hat{x}$ and the desired line orientation $\hat{\xi}$. Taking θ as the angle between $\hat{\xi}$ and the x-axis, $\theta = 0^\circ$ corresponds to a screw dislocation and $\theta = 90^\circ$ is an edge dislocation.

Once the system is equilibrated, the top surface is displaced along $\hat{x}$ to increase the shear stress. The stress required to move the dislocation is recorded as the Peierls stress. Fig. 10(a) shows how $\tau_{\rm Peierls}$ varies with $b_{\rm core}/d$ for different angles. Panel (b) shows the angular variation of $\tau_{\rm Peierls}$ at fixed $b_{\rm core}$, where the case $b_{\rm core}/d = 1.8$ corresponds to Fig. 9.

As expected from Eq. 18, the Peierls stress drops roughly exponentially with $b_{\rm core}$ for edge dislocations. The prefactor in the exponential depends strongly on the orientation, with screw dislocations the most difficult to depin. The Peierls stress shows additional peaks for edge dislocations and for mixed character dislocations at 45°. Other angles have similar values of $\tau_{\rm Peierls}$ and show a very rapid drop with increasing core width.

The solid gray lines in Fig. 9 show the local Peierls stress from Fig. 10 for (a) edge and (b) screw dislocations at the local pressure. Even though the systems are near the point where dislocations move, the stress at each core is lower than the corresponding Peierls stress. The stress is about half the expected Peierls stress for edge dislocations, where the stress in the core is near $\tau_{\rm max}$, signalling a nearly unstable state. Note that the dislocations sample all orientations from edge to screw and for $b_{\rm core}/d = 1.8$ most angles have $\tau_{\rm Peierls}$ seven times smaller

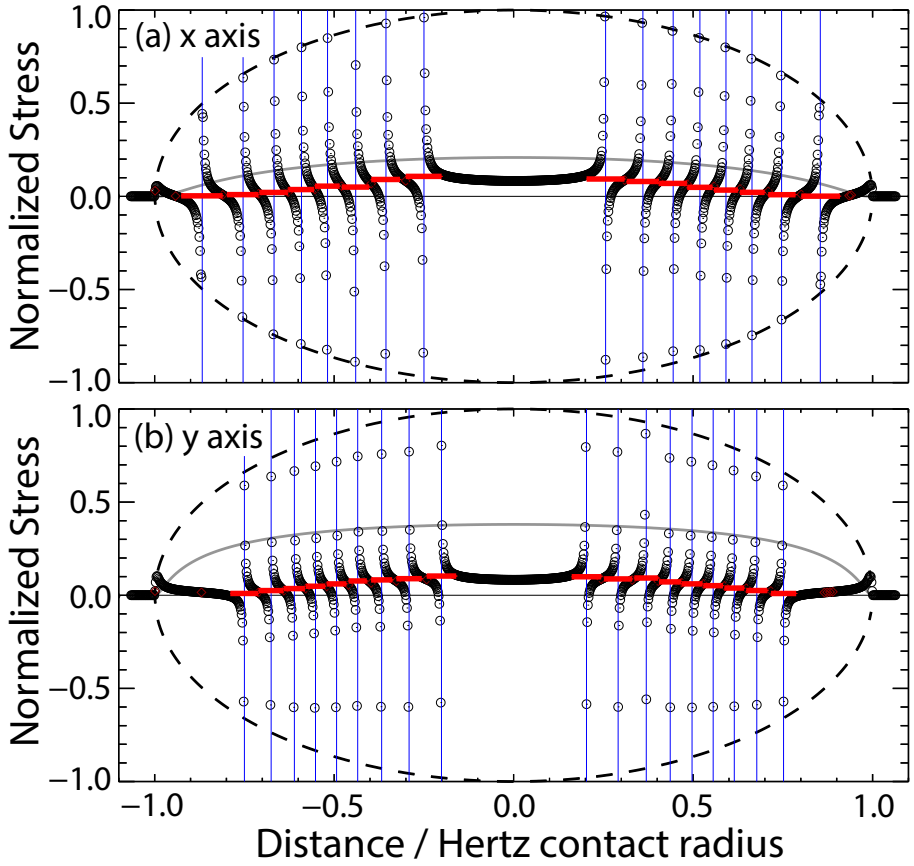

FIG. 9: Variation in shear stress (circles) across the contact for atoms along the (a) x-axis (sliding direction) and (b) y-axis (transverse direction) for the lateral force model in Regime III. Stresses are normalized by αp_0 and position by the Hertz contact radius. Vertical solid lines indicate dislocation cores and dashed lines indicate the bounds on the local shear stress, $\pm\alpha p$. Horizontal red bars indicate the mean local stress acting on each dislocation and are determined by averaging the stress an equal distance on both sides of the dislocation. A solid gray curve indicates the calculated Peierls stress for the given pressure, which is larger for screw dislocations.

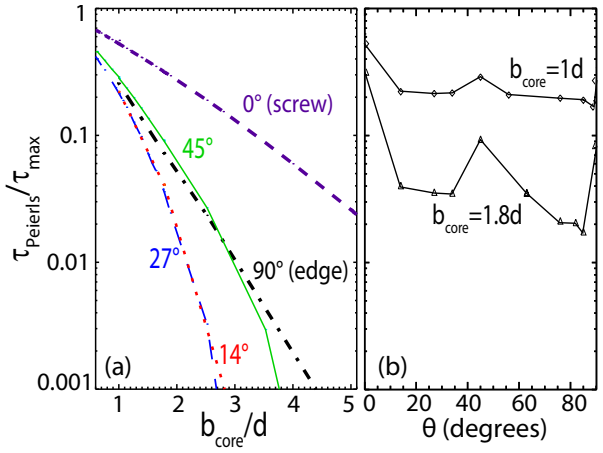

FIG. 10: The Peierls stress for edge and screw and mixed character dislocations in the lateral force model as a function of (a) core width and (b) dislocation character. The character is labeled as the angle between the line direction $\hat{\xi}$ and the Burgers vector $\boldsymbol{b} = d\hat{x}$.

than for screw dislocations and less than half that for edge dislocations. This is one reason the system in Fig. 9 is nearly unstable even though the edge and screw dislocations are below the independently calculated τ_{Peierls}. A second is that the stress to move dislocations decreases with increasing density of dislocations due to dislocation interactions. In general, for both the case considered here and the adhesive systems seen in Ref. 21, we find that the onset of motion is close to, but smaller than, the Peierls stress for edge dislocations.

We conclude by using these results to estimate the friction in Regime III. Fitting to the edge dislocation results in Fig. 10 we find $k_1 = 1.5$ and $k_2 = 1.6$. As just discussed, the onset of motion occurs at about half of the Peierls stress for edge dislocations. In addition, Eq. 20 uses the core radius at the center of the contact rather than integrating over the changing core size. The blue dotted lines in Fig. 4 show the prediction using a numerical integration over the contact of half the Peierls stress to account for these two effects. The lines clearly capture the available data in the regime where μ rises. Larger sys-

tems would be needed for a more complete test of this scaling.

IV. CONCLUSIONS

We have considered the prototypical case of sphere on flat contact over contact and sphere radii from nanometers to micrometers. A previous study considered the case of a constant shear stress within the contact, as is often assumed for adhesive contacts. Here we use repulsive interactions between identical crystals that naturally produce a local shear stress that is proportional to pressure, $\tau_{\max} = \alpha p$, as assumed in the Cattaneo-Mindlin contact theory. Results from an explicit model of a spherical tip are compared to a lateral force model that removes the effects of curvature and has a different local periodic potential. Despite these differences, results from the two models fall on the same dimensionless plot in Fig. 4. This supports the conclusion that the regimes we identify are generic.

The key scaling parameter is the ratio of the contact radius to the core width of edge dislocations. The core width gives the minimum distance along the contact for the registry between surfaces to change by an interatomic spacing d. The core width decreases with increasing pressure and we use the value $b^0_{\rm core}$ from the center of the contact where the pressure is highest.

In Regime I, the contact size is less than $b^0_{\rm core}$, so all atoms must advance nearly in registry. The total friction force is just the sum of periodic forces on each atom. Each is proportional to the local normal force so we get a constant coefficient of static friction $\mu = \alpha$. The kinetic friction is the average of the periodic force and is nearly zero.

In Regime II, the contact size is larger than $b^0_{\rm core}$. The large shear stress and low pressure at the edge of the contact lead to nucleation of a dislocation there. The dislocation is unstable and rapidly moves to the center of the contact where it annihilates. This rapid instability is evident in plots of force vs. displacement which show classic stick-slip behavior - gradual increases followed by rapid drops. The drops decrease in size as $a/b^0_{\rm core}$ increases and the kinetic friction approaches the static friction.

The Cattaneo-Mindlin theory does not include the characteristic lengths d and $b^0_{\rm core}$. As a result, it predicts kinks in the shear stress and interfacial displacement. In our simulations, these kinks are smeared over a width corresponding to the local core width which depends on radius and the character of the dislocation. Screw dislocations at the top and bottom of the contact have narrower widths than edge dislocations at the front and back of the contact. As a result the stress field has higher peaks at the top and bottom and screw dislocations nucleate first. Recent experiments on elastomer tips find a related instability nucleates at the top and bottom of sliding contacts.[40]

A scaling relation was developed for μ/α in Regime II by finding the radius where the shear stress at a distance $b_{\rm core}$ from the edge of the contact equals the maximum shear stress associated with the pressure at that same radius. From Eq. 16, μ/α drops as the -2/3 power of $\alpha a^2/dR$. This is in sharp contrast to the corresponding result for adhesive contacts where the shear stress drops as the -1/2 power of a and the sphere radius does not matter. Expressing the scaling in terms of normal load, μ/α drops as load to the -4/9 power.

In Regime III, many dislocations remain stuck in the contact before the system becomes unstable. Stick-slip friction is observed with kinetic friction close to the static friction. The friction force is related to the Peierls stress required to advance the dislocation array. Using standard results for the Peierls stress we find $\mu/\alpha \propto \exp(-R/c\alpha a)$. Thus increasing a by increasing the load leads to an increase in friction coefficient. This interesting regime is only evident for very large contacts (Eq. 19). A full characterization of the dislocation arrays is complicated because the Peierls stress varies with angle around each dislocation loop and there are large, long-range interactions between dislocations.

One important simplification in our work is use of aligned, identical lattices on the two surfaces. This assumption is necessary to satisfy the assumptions of Hurtado and Kim's theory and is an interesting special case. However real surfaces are likely to be misaligned, and curvature and Poisson effects can lead to mismatch in registry even when the initial surfaces are in registry. These cases were considered in our previous study of adhesive surfaces and we find similar results for repulsive interactions. In cases corresponding to Regime I, lack of registry leads to values of μ/α that are less than unity and decrease with a. When $a > b_{\rm core}$, misalignment leads to dislocations without the nead for nucleation. The friction drops to the Peierls stress expected for Regime III.

The local shear stress between real surfaces may not be simply proportional to load or area. For example, many surfaces[1,5,8,12,25,43] follow a linear combination: $\tau_{\max} = \tau_0 + \alpha p$. The same three regimes of scaling will occur for this general case, but there will be no simple scaling of the total friction with area or load and no single power law characterizing the relation between friction and contact radius. Analysis of dislocations for this general case may borrow from studies of bulk dislocations with a pressure-dependent γ-surface (also known as the generalized stacking fault energy).[44,45]

Our results focus on the quasistatic limit. Other effects may become important at finite velocity. For example, Ref.[46] considered quasi-1D incommensurate systems pulled over a substrate at finite velocity. Superlubricity was destroyed for systems longer than a critical length, because the viscous drag force led to a change in lattice constant and made the surfaces commensurate. While this mechanism is different and the critical length diverges as velocity goes to zero, these results also show the important role of elasticity in modifying friction.

Another important limitation of our results is that the

substrate is treated in the elastic limit. Surface stresses may lead to plastic deformation inside the bulk of the contacting solids rather than at the interface. This would depend on the loading configuration, orientations of slip planes, and the relative strength of interactions across the interface and in the bulk. It would be most likely for identical materials contacting on a crystal plane where slip is difficult.

Acknowledgments

This paper is based upon work supported by the National Science Foundation under Grant No. DMR-1411144 and by the Deutsche Forschungsgemeinschaft (grant PA 2023/2). Computations were carried out on the Johns Hopkins Homewood High Performance Cluster, Maryland Advanced Research Computing Center and the Jülich Supercomputing Center (grant hfr13).

* Electronic address: lars.pastewka@imtek.uni-freiburg.de
† Electronic address: mr@pha.jhu.edu

[1] F. P. Bowden and D. Tabor, *The Friction and Lubrication of Solids* (Oxford : Clarendon Press, 1964), ISBN 0198507771.
[2] K. L. Johnson, *Contact Mechanics* (Cambridge University Press, 1985), http://dx.doi.org/10.1017/cbo9781139171731.
[3] F. J. Giessibl, Reviews of modern physics **75**, 949 (2003).
[4] M. Kappl and H.-J. Butt, Particle & Particle Systems Characterization **19**, 129 (2002).
[5] J. Israelachvili, Y. Min, M. Akbulut, A. Alig, G. Carver, W. Greene, K. Kristiansen, E. Meyer, N. Pesika, K. Rosenberg, et al., Reports on Progress in Physics **73**, 036601 (2010).
[6] J. Greenwood and J. Williamson, in *Proceedings of the Royal Society of London A: Mathematical, Physical and Engineering Sciences* (The Royal Society, 1966), vol. 295, pp. 300–319.
[7] I. L. Singer, H. M. Pollack, and O. Vingsbo, *Fundamentals of Friction: Macroscopic and Microscopic Processes (NATO Advanced Science Institute Series, Series E: Applied Sciences, Vol. 220)*, vol. 61 (ASME International, 1994), http://dx.doi.org/10.1115/1.2901414.
[8] A. Berman, C. Drummond, and J. N. Israelachvili, Tribol. Lett. **4**, 95 (1998).
[9] A. M. Homola, J. N. Israelachvili, P. M. McGuiggan, and M. L. Gee, Wear **136**, 65 (1990).
[10] R. W. Carpick, N. Agrait, D. F. Ogletree, and M. Salmeron, Langmuir **12**, 3334 (1996).
[11] M. A. Lantz, S. J. O'Shea, M. E. Welland, and K. L. Johnson, Phys. Rev. B **55**, 10776 (1997).
[12] B. J. Briscoe, Philos. Mag. A **43**, 511 (1981).
[13] *Fundamentals of Friction: Macroscopic and Microscopic Processes* (Elsevier, Amsterdam, 1992).
[14] J. A. Hurtado and K.-S. Kim, Proceedings of the Royal Society A: Mathematical, Physical and Engineering Sciences **455**, 3363 (1999), http://dx.doi.org/10.1098/rspa.1999.0455.
[15] J. A. Hurtado and K.-S.Kim, Proceedings of the Royal Society A: Mathematical, Physical and Engineering Sciences **455**, 3385 (1999), http://dx.doi.org/10.1098/rspa.1999.0456.
[16] J. P. Hirth and J. Lothe, *Theory of Dislocations* (John Wiley & Sons, 1982).
[17] R. W. Carpick, N. Agrait, D. F. Ogletree, and M. Salmeron, J. Vac. Sci. Technol. B **14**, 1289 (1996).
[18] Y. Gao, Journal of the Mechanics and Physics of Solids **58**, 2023 (2010), http://dx.doi.org/10.1016/j.jmps.2010.09.014.
[19] C. Campaná and M. H. Müser, Physical Review B **74**, 075420 (2006).
[20] L. Pastewka, T. A. Sharp, and M. O. Robbins, Physical Review B **86**, 075459 (2012), http://dx.doi.org/10.1103/physrevb.86.075459.
[21] T. A. Sharp, L. Pastewka, and M. O. Robbins, Physical Review B **93**, 121402 (2016).
[22] M. Hirano and K. Shinjo, Phys. Rev. B **41**, 11837 (1990).
[23] M. H. Müser, L. Wenning, and M. O. Robbins, Phys. Rev. Lett. **86**, 1295 (2001).
[24] D. Dietzel, C. Ritter, T. Möninghoof, H. Fuchs, A. Schirmeisen, and U. D. Schwarz, Phys. Rev. Lett. **101**, 125505 (2008).
[25] J. Ringlein and M. O. Robbins, American Journal of Physics **72**, 884 (2004).
[26] M. H. Müser, M. Urbakh, and M. O. Robbins, Advances in Chemical Physics **126**, 187 (2003).
[27] J. A. Harrison, S. J. Stuart, and D. W. Brenner, in *Handbook of Micro/Nanotribology*, edited by B. Bhushan (CRC Press, Boca Raton, FL, 1999), pp. 525–594.
[28] J. Li and E. J. Berger, Journal of Elasticity **63**, 137 (2001).
[29] R. W. Hockney, Tech. Rep., Langley Research Center, Hampton, Va. (1970).
[30] L. Pastewka and M. O. Robbins, Applied Physics Letters **108**, 221601 (2016).
[31] E. Bitzek, P. Koskinen, F. Gähler, M. Moseler, and P. Gumbsch, Phys. Rev. Lett. **97**, 170201 (2006).
[32] J. Ringlein and M. O. Robbins, American Journal of Physics **72**, 884 (2004).
[33] P. A. Thompson and M. O. Robbins, Science **250**, 792 (1990).
[34] H. Hertz, J. reine angew. Math **92**, 110 (1881).
[35] B. Luan and M. O. Robbins, Nature **435**, 929 (2005), http://dx.doi.org/10.1038/nature03700.
[36] B. Luan and M. O. Robbins, Physical Review E **74**, 026111 (2006).
[37] O. M. Braun and Y. S. Kivshar, *The Frenkel-Kontorova*

Model: Concepts, Methods, and Applications (Springer Science & Business Media, 2004).
[38] S. Cheng, B. Luan, and M. O. Robbins, Physical Review E **81**, 016102 (2010).
[39] R. W. Carpick and M. Salmeron, Chem. Rev. **97**, 1163 (1997).
[40] M. C. Audry, C. Fretingny, A. Chateauminois, J. Teissere, and E. Barthel, Eur. Phys. J. E **35**, 83 (2012).
[41] J. R. Rice, Journal of the Mechanics and Physics of Solids **40**, 239 (1992).
[42] F. Nabarro, Materials Science and Engineering: A **234-236**, 67 (1997), http://dx.doi.org/10.1016/S0921-5093(97)00184-6.
[43] H. Yoshizawa, Y.-L. Chen, and J. N. Israelachvili, J. Phys. Chem. **97**, 4128 (1993).
[44] V. Vitek, Philosophical Magazine **18**, 773 (1968).
[45] J. Amodeo, P. Carrez, and P. Cordier, Philosophical Magazine **92**, 1523 (2012).
[46] M. Ma, A. Benassi, A. Vanossi, and M. Urbakh, Phys. Rev. Lett. **114**, 055501 (2015).
[47] The analytic GF used in other simulations was sampled and inverse Fourier transformed.